Validation of x-ray microfocus computed tomography as an imaging tool for porous structures

G. Kerckhofs, J. Schrooten, T. Van Cleynenbreugel, S. V. Lomov, and M. Wevers

Related Articles

Combined resistive and laser heating technique for in situ radial X-ray diffraction in the diamond anvil cell at high pressure and temperature
Rev. Sci. Instrum. 84, 025118 (2013)

The Oxford-Diamond In Situ Cell for studying chemical reactions using time-resolved X-ray diffraction
Rev. Sci. Instrum. 83, 084101 (2012)

Synchrotron-based ultrafast x-ray diffraction at high repetition rates
Rev. Sci. Instrum. 83, 063303 (2012)

Shortening x-ray pulses for pump-probe experiments at synchrotrons
J. Appl. Phys. 109, 126104 (2011)

High-pressure and high-temperature x-ray diffraction cell for combined pressure, composition, and temperature measurements of hydrides
Rev. Sci. Instrum. 82, 065108 (2011)

Additional information on Rev. Sci. Instrum.

Journal Homepage: http://rsi.aip.org

Journal Information: http://rsi.aip.org/about/about_the_journal

Top downloads: http://rsi.aip.org/features/most_downloaded

Information for Authors: http://rsi.aip.org/authors

Validation of x-ray microfocus computed tomography as an imaging tool for porous structures

G. Kerckhofs,[1,a)] J. Schrooten,[1] T. Van Cleynenbreugel,[2,3] S. V. Lomov,[1] and M. Wevers[1]

[1]*Department of Metallurgy and Materials Engineering, Katholieke Universiteit Leuven, Kasteelpark Arenberg 44-bus 2450, B-3001 Leuven, Belgium*
[2]*Division of Biomechanics and Engineering Design, Katholieke Universiteit Leuven, Celestijnenlaan 300C, B-3001 Leuven, Belgium*
[3]*Materialise Dental NV, Technologielaan 15, B-3001 Leuven, Belgium*

X-ray microfocus computed tomography (micro-CT) is recently put forward to qualitatively and quantitatively characterize the internal structure of porous materials. However, it is known that artifacts such as the partial volume effect are inherently present in micro-CT images, thus resulting in a visualization error with respect to reality. This study proposes a validation protocol that in the future can be used to quantify this error for porous structures in general by matching micro-CT tomograms to microscopic sections. One of the innovations of the protocol is the opportunity to reconstruct an interpolated micro-CT image under the same angle as the physical cutting angle of the microscopic sections. Also, a novel thresholding method is developed based on matching micro-CT and microscopic images. In this study, titanium porous structures are assessed as proof of principle. It is concluded for these structures that micro-CT visualizes 89% of the total amount of voxels (solid and pore) correctly. However, 8% represents an overestimation of the real structure and 3% are real structural features not visualized by micro-CT. When exclusively focusing on the solid fraction in both the micro-CT and microscopic images, only an overestimation of about 5% is found. © *2008 American Institute of Physics.* [DOI: 10.1063/1.2838584]

I. INTRODUCTION

Porous materials are ubiquitous in modern life: in chemical industry as filter materials, in buildings as insulation or heat exchangers, or even in the human body as cancellous bone or porous scaffolds for tissue engineering. In order to understand and simulate the functional behavior of these materials, a correct visualization and description of the morphology is desired. X-ray microfocus computed tomography (micro-CT) is recently put forward by many researchers to qualitatively and quantitatively characterize the internal structure of porous materials. It provides a means to acquire a complete three-dimensional (3D) image of the structure visualizing the internal architecture at the microscopic level in a nondestructive way. Additionally, the micro-CT images enable subsequent image analysis, resulting in a 3D quantification of the internal structure. However, although micro-CT is widely used in diverse scientific fields[1–8] and most advantages and limitations are known,[9,10] one of the prerequisites for correct analysis of the micro-CT data is to ensure and quantify the accuracy and reliability of the images used. It is known that artifacts such as the partial volume effect (PVE) are inherently present in micro-CT images, thus resulting in a visualization error with respect to reality. But how large is this error and how does it express itself?

The accuracy of micro-CT depends on various factors. When the equipment itself is concerned, the focal spot as well as the detector can limit the attainable spatial resolution. Also, the specimen size and selected region of interest (ROI) influence the voxel size of the images. Since for example the PVE depends directly on the resolution, the accuracy of the images goes down with lower resolution. Currently, attainable spatial resolutions lie in the range of 10 μm for *standard* micro-CT, in the range of $1-2$ μm for *high resolution* standard, and *synchrotron* micro-CT, and in the range of $0.4-0.6$ μm for *nano*-CT.[11] Currently, standard micro-CT is still the most widely used form of micro-CT and is applied in this work. For cancellous bone, having a global porosity between 50% and 90% and having trabeculae with thicknesses between 100 and 200 μm, the spatial resolution of standard micro-CT is sufficient to accurately visualize the surface of individual trabeculae, as stated by Muller *et al.*[12] However, architectures with structural features in the same order of magnitude as the focal spot or voxel size, for example, thin struts or micropores, are difficult to be visualized accurately leading to an erroneous analysis.

The image quality (e.g., the contrast in the images) depends among other things on the material and architecture of the specimen. Metals, for example, generally cause artifacts such as streaks, beam hardening, PVE, and scattering[13,14] more pronounced than ceramics, resulting in less image quality meaning less accuracy. Low density polymers, on the

---

a)Author to whom correspondence should be addressed. Tel: +32 16321193. FAX: +32 16321990. Electronic mail: greet.kerckhofs@mtm.kuleuven.be. Postal address: Kasteelpark Arenberg 44 bus 2450, 3001 Heverlee, Belgium.
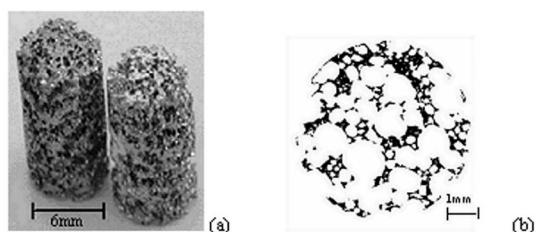
FIG. 1. (a) A typical cylindrical porous titanium structure with a mean radius of 3.00 ± 0.05 mm, a mean height of 10.0 ± 0.1 mm, and a global porosity of about 80%, and (b) an optical light microscopy image of a typical cross section of such a sample.

other hand, need quite extreme acquisition parameters (low voltage and current), leading to less contrast and hence also to less image quality.

The best-known validation technique for micro-CT when applied to porous structures is the case of bone where comparison is made with histology by comparing the structural parameters.[15–23] Although this validation protocol is considered as the "golden standard," it still contains several shortcomings. First, histological sectioning and staining is used for the assessment of biological tissues. Thus, when porous materials in general are addressed, for example, aluminium heat exchangers, it cannot be applied but similar metallographic sample preparation and image analysis need to be performed. Additionally, it was found in literature that up to now, when the physical cutting angle of the histological sections does not coincide with the reconstruction angle of the micro-CT images, no interpolation is made. Instead, the micro-CT image that resembles the histological section the best is considered for the matching. This can already give rise to a mismatch.[15,16,18] Also, most studies compare micro-CT to histology based on structural parameters. However, as also stated by Stoppie *et al.*,[23] it is a misunderstanding that a good correlation between structural parameters should necessarily mean identical images.

Thus, although micro-CT is extensively used for the characterization of porous materials, the accuracy and the reliability of the images still needs quantification. The goal of this work is to establish a protocol for the validation of micro-CT as an imaging tool for porous structures by matching micro-CT tomograms to microscopic sections. A set of validation parameters can be defined per set of acquisition parameters, determined for a particular sample (material, geometry, and dimensions) on a particular micro-CT device, and for images with a comparable spatial resolution. One of the innovations of the protocol is the possibility to reconstruct an interpolated micro-CT image under the same angle as the physical cutting angle of the microscopic sections. Additionally, a novel thresholding method is developed based on matching the micro-CT and microscopic images.

II. MATERIALS AND METHODS

A. Sample material

In this study, cylindrical porous titanium structures with thin struts (Fig. 1) are selected as a first material to investigate the validation protocol. These cylinders have a

TABLE I. Characteristics of the Philips HOMX 161 x-ray system with AEA TOMOHAWK CT software.

X-ray source voltage	15–160 kV
Maximum current	3.2 mA
Microfocal spot	From 5 to 200 μm
Minimum spatial resolution	10 μm (5 μm voxel size)
Detector	CCD camera with a resolution of 1024×1024 pixels and a 12 bit dynamic range
Maximum sample dimensions	20 cm width and 20 cm height

mean radius of 3.00 ± 0.05 mm and a mean height of 10.0 ± 0.1 mm [supplied by VITO (Mol, Belgium)]. They are produced by gel casting,[24,25] resulting in porous structures with struts ranging from 20 to 100 μm, pores ranging from 50 to 500 μm and a global porosity of about 80%. The broad range in strut thickness and pore size is preferred to address structural elements much larger than the attainable spatial resolution together with the smallest possible structural elements to be visualized by micro-CT in the same sample.

B. Micro-CT equipment

In micro-CT, contrary to medical CT, the sample is rotated between a fixed x-ray source and detector. The source generates a polychromatic spectrum where the x-ray intensity is a function of the photon energy. The spectrum depends on the acquisition parameters, namely, the voltage, the current, and the applied filter material. The polychromatic x-rays pass through the sample where they are attenuated. The intensities of the attenuated x-rays are measured by the detector, and by applying a mathematical algorithm[26] on these measurements, gray-level images representing the attenuation inside the sample are reconstructed. In case of 8-bit images, the gray levels range from 0 to 255 representing the minimum and maximum intensities respectively. The resultant images are two-dimensional (2D) and show the geometry of the sample in the plane of the cross section. A series of 2D images can then be combined to create a 3D representation of the sample. A more detailed description of the technique can be found in Refs. 26–28. For this study, a Philips HOMX 161 x-ray system with AEA TOMOHAWK CT software is used. Table I shows the characteristics of the device.

C. Validation protocol

The validation protocol can be divided into six parts, as shown in Fig. 2, namely, (1) acquisition of a set of micro-CT images of the full sample, (2) metallographic preparation of the sample and digitizing by microscopy, (3) fitting a micro-CT image to the microscopic image, followed by the reconstruction of an interpolated micro-CT image when required, (4) registration of the microscopic to the interpolated micro-CT image, (5) binarization of the interpolated micro-CT image, and (6) matching the interpolated micro-CT to the microscopic image. In the following, the six steps are elaborated when applied to the selected titanium porous structures.
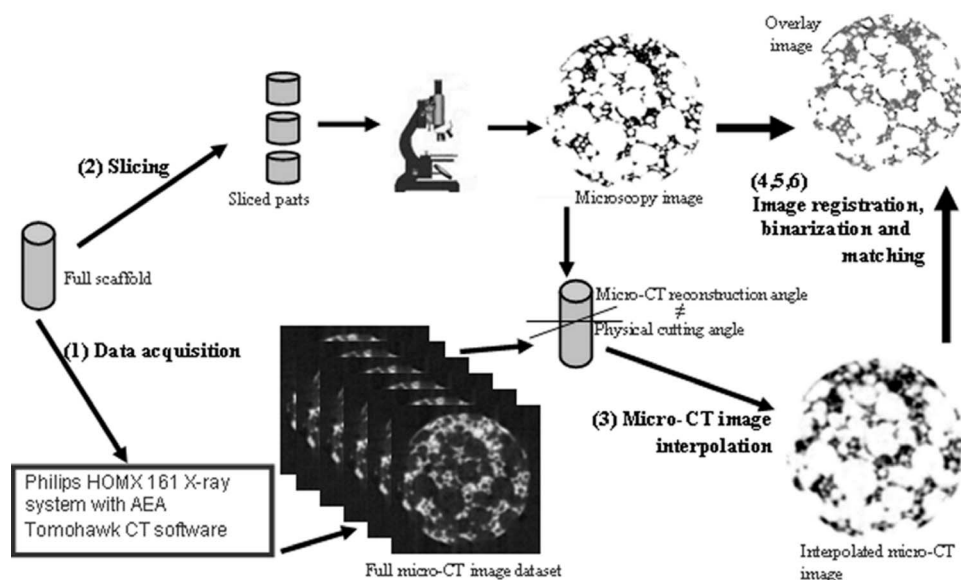
FIG. 2. Schematic overview of the validation protocol, consisting of six parts: (1) acquisition of a set of micro-CT images of the full sample, (2) metallographic preparation of the sample and digitizing by microscopy, (3) fitting a micro-CT image to the microscopic image, followed by the reconstruction of an interpolated micro-CT image when required, (4) registration of the microscopic to the interpolated micro-CT image, (5) binarization of the interpolated micro-CT image, and (6) matching the microscopic to the interpolated micro-CT image.

1. Data acquisition by means of micro-CT

The sample is mounted on a sample holder and positioned on the rotation table ensuring that the cylinder axis coincides with the rotation axis of the scanner rotation table. An upgrade of a CT simulator,[29] originally developed by De Man *et al.*,[13] is applied as an objective method to select optimal acquisition parameters (voltage, current, and filter material) and, thus, overcoming a trial and error approach. Table II summarizes the applied acquisition parameters. The radiographic images are 16-bit tiff files with gray values in the range of 0–65 536, while the reconstructed axial micro-CT images are 8-bit bitmaps with gray values ranging from 0 to 255.

2. Metallographic preparation

After scanning, the sample is embedded in a resin (Epofix 4004) and sectioned in three parts with a Buehler Isomet low speed precision sectioning saw. The created surfaces are grinded and polished, and digitized using a Leitz Metalloplan optical light microscope resulting in images with a spatial resolution of 3.0 μm. It should be mentioned that, for example, for materials with a low contrast ratio between material and resin or when a higher resolution is desired, scanning electron microscopy (SEM) can also be applied. The obtained microscopic images are considered the "exact" architecture and are compared to the micro-CT im-

TABLE II. Acquisition parameters for porous titanium structures on a Philips HOMX 161 x-ray system with AEA TOMOHAWK CT software.

Voltage[a]	90 kV
Current[a]	0.39 mA
Filter material[a]	1 mm aluminium
Spatial resolution	27 μm (13.5 μm voxel size)
Rotation step, rotation angle	0.5° over 187°
Frame averaging	32 frames
Amount of axial micro-CT slices	About 900
Slice thickness	1 voxel (=13.5 μm)

[a]Determined by means of a micro-CT simulator.

ages in the same plane as the sections. The resulting microscopic images are manually segmented which is straightforward because of the distinct difference in gray levels between the pore space and the material.

3. Image interpolation

Due to the possible difference between the physical cutting angle of the metallographic sections and the reconstruction angle of the micro-CT images, a mismatch can already appear between the microscopic and the corresponding micro-CT image. Therefore, the position and inclination of the microscopic image within the micro-CT data set need to be identified to be able to reconstruct an interpolated micro-CT image at the same position under the same angle. This is done in MATLAB using the image processing toolbox. The in-house developed routine asks the user to point out markers in the micro-CT data set which are also present in the microscopic image, for example, certain pores or particular struts. By fitting a least squares fit plane through these markers, an interpolated micro-CT image is reconstructed.

4. Image registration

The microscopic images have a spatial resolution which is about nine times higher than the interpolated micro-CT images. Also, the in-plane orientation of the microscopic images can differ from the one of the interpolated micro-CT images. Hence, a so-called "registration" is performed to match the spatial resolution, to reorient and/or to translate the microscopic images according to the interpolated micro-CT images. Maes *et al.*,[30,31] have developed an automatic image registration tool based on mutual information which allows two images to be automatically and user independently registered. This image registration tool is applied in this study to register the microscopic to the corresponding, interpolated micro-CT images.

5. Image segmentation

Because micro-CT images are gray-level images, the most critical part in the validation protocol is finding the optimal threshold for binarization. As shown in Refs. 16 and 32–34, the threshold has a significant influence on the image-based structural analysis. The most widely applied threshold techniques use a global threshold. A single threshold value is selected, in this study ranging between 0 and 255, which typically represents the intensity value that optimally distinguishes the pore from the solid phase. As a result, a binary image is generated. Many thresholding methods and algorithms were developed over the years, depending on the material used, the application, the quality, and/or noise level of the images, etc.[32,35–38] Several review articles discuss and evaluate a range of threshold methods.[39–42] However, they all conclude the same: that finding the optimal threshold is not a trivial issue and that there is no single threshold algorithm that is successful for all possible image variations in the spatial domain.

In this study, a novel thresholding method is developed based on matching microscopic with their corresponding, interpolated micro-CT images. Microscopic images are 2D entities consisting of pixels (picture elements). Micro-CT images, on the other hand, are 3D entities expressed in voxels (volume elements) with a certain thickness. As mentioned in Table II, in this research the thickness of the micro-CT images is kept minimal which results in cubic voxels, thus no averaging is made over the thickness. To prevent confusion, from now on the pixels in the microscopic images and the voxels in the micro-CT images are referred to as "elements."

When overlaying both the microscopic and their corresponding, interpolated micro-CT images, the optimum is represented by a maximum in coinciding and a minimum in noncoinciding solid elements. By altering the threshold value for the micro-CT images, this optimum can be approximated. Per set of microscopic and corresponding, interpolated micro-CT image (=image set), the threshold approximating the optimum the closest, named the "best" threshold, is determined. By averaging the "best" threshold values over a significant amount of image sets, the "optimal" threshold is defined. This "optimal" threshold is only valid for the selected material, micro-CT device and acquisition parameters. If one of these settings changes significantly, a new "optimal" threshold needs to be determined.

One of the major advantages of this novel thresholding method is that it accounts for closed pores, in contrast with the Archimedes method.[32,43] Also, since the physical visualization of the structure is taken as a reference, it results in binary images closely representing the real structure. It is a time-consuming procedure, but once the "optimal" threshold is determined for certain settings, it can be used for further research. Still, an important limitation of the method is that it is a global thresholding method and, hence, it does not locally account for the errors present in micro-CT images due to the limited spatial resolution, PVE, etc. However, since this thresholding method is linked to the proposed validation protocol, this error can be quantified.
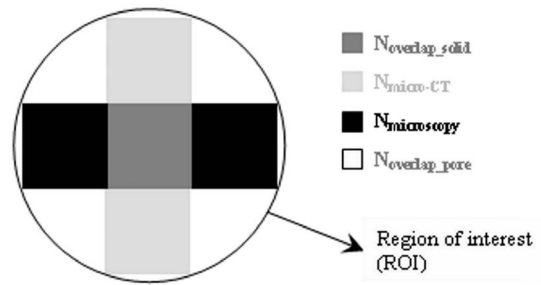

FIG. 3. Simplification of an overlay image where the overlapping solid elements are displayed in dark gray, the noncoinciding solid elements in the microscopic image in black and the noncoinciding solid elements in the micro-CT image in light gray. The white background represents pore space. The ROI is in this case defined as the circle with a diameter of 3.00 mm surrounding the material present in the both the microscopic and the corresponding, interpolated micro-CT image.

6. Matching

Both the binarized microscopic and corresponding, interpolated micro-CT images are matched and overlaid, resulting in images displaying the overlapping solid elements in dark gray, the noncoinciding solid elements in the microscopic image in black and the noncoinciding solid elements in the micro-CT image in light gray. The white background represents pore space. Figure 3 shows a simplification of an overlay image. The number of elements in each color is counted, yielding the amount of solid elements in the micro-CT image not coinciding with the solid elements in the microscopic image ($N_{\text{micro-CT}}$), the amount of solid elements in the microscopic image not coinciding with the solid elements in the micro-CT image ($N_{\text{microscopy}}$), the amount of coinciding solid elements ($N_{\text{overlap\_solid}}$), and the amount of coinciding pore elements ($N_{\text{overlap\_pore}}$). N_{total} represents the total amount of elements present in the ROI. In this case, the ROI is defined as the circle with a radius of 3.00 mm surrounding the material present in both the microscopic and the corresponding, interpolated micro-CT image.

The following parameters are defined:

- total amount of solid elements present in the micro-CT image (elements),

$$N_{\text{micro-CT}}^{\text{tot}} = N_{\text{overlap\_solid}} + N_{\text{micro-CT}}; \quad (1)$$

- total amount of solid elements present in the microscopic image (elements),

$$N_{\text{microcopy}}^{\text{tot}} = N_{\text{overlap\_solid}} + N_{\text{microscopy}}; \quad (2)$$

- percentage in solid overlap (%),

$$\text{Overlap}_{\text{solid}} = \left[\frac{N_{\text{overlap\_solid}}}{N_{\text{microscopy}}^{\text{tot}}} \right] \cdot 100; \quad (3)$$

- percentage in solid micro-CT mismatch (%),

$$M_{\text{micro-CT\_solid}} = \left[\frac{N_{\text{micro-CT}}}{N_{\text{microscopy}}^{\text{tot}}} \right] \cdot 100; \quad (4)$$

- percentage in solid microscopic mismatch (%),

$$M_{\text{microscopy\_solid}} = \left[\frac{N_{\text{microscopy}}}{N_{\text{microscopy}}^{\text{tot}}} \right] \cdot 100; \quad (5)$$
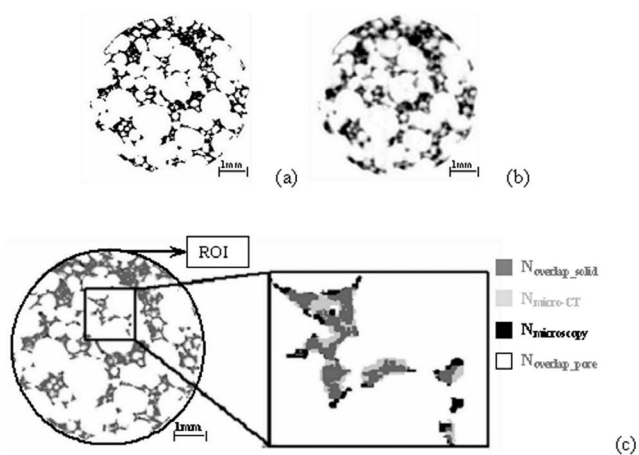
FIG. 4. For a particular titanium porous sample (Φ 6 mm): (a) the microscopic image of a metallographic slice, (b) the corresponding, interpolated micro-CT image, and (c) the resulting match of both.

- percentage in total solid mismatch (%),

$$M_{\text{total\_solid}} = M_{\text{micro-CT\_solid}} + M_{\text{microscopy\_solid}}; \tag{6}$$

- percentage in total overlap (%),

$$\text{Overlap}_{\text{total}} = \left[\frac{N_{\text{overlap\_solid}} + N_{\text{overlap\_pore}}}{N_{\text{total}}} \right] \cdot 100; \tag{7}$$

- percentage in total micro-CT mismatch (%),

$$M_{\text{micro-CT\_total}} = \left[\frac{N_{\text{micro-CT}}}{N_{\text{total}}} \right] \cdot 100; \tag{8}$$

- percentage in total microscopic mismatch (%),

$$M_{\text{microscopy\_total}} = \left[\frac{N_{\text{microscopy}}}{N_{\text{total}}} \right] \cdot 100; \tag{9}$$

- percentage in total mismatch (%),

$$M_{\text{total}} = M_{\text{micro-CT\_total}} + M_{\text{microscopy\_total}}. \tag{10}$$

For the determination of the "optimal" threshold, only the solid elements in both the microscopic and the micro-CT images are considered for matching since artifacts like beam hardening and the PVE reflect only on the solid elements

(when biphasic images are assessed). The solid elements in the microscopic image are taken as reference [Eq. (3)–(6)]. However, since image-based structural analysis is performed on the total image containing solid and pore elements, the total overlap and mismatch are determined inside the ROI taking into account the pore elements. The total amount of elements inside the ROI is then taken as reference [Eq. (7)–(10)].

III. RESULTS

In total 36 interpolated micro-CT images are matched to their corresponding microscopic images. Figure 4 shows an example of (a) a microscopic image of a metallographic section, (b) the corresponding, interpolated micro-CT image, and (c) the resulting match of both.

A. Statistical analysis

All results are expressed as mean $\pm$ standard deviation. The normality of the variables is assessed using the Kolmogorov–Smirnov test. Values smaller than 1.5 times the interquartile range (IQR) and larger than three times the IQR are defined as outliers and are, in this study, excluded for assessing the mean $\pm$ standard deviation. The IQR computes the difference between the 75th and the 25th percentiles of variable. The IQR is a robust estimate of the spread of the data, since changes in the upper and lower 25% of the data do not affect it. The correlation between two variables is assessed using the Pearson's correlation test. Statistical analysis is done using a statistical software add-in for MICROSOFT® EXCEL® for Windows, namely, ANALYSE-IT version 1.73.

B. "Optimal" threshold

As mentioned before, the "best" threshold is defined where the solid overlap minus total solid mismatch reaches its maximum. Figure 5(a) indicates for one particular image set that the total solid mismatch reaches a minimum at a certain threshold value, in this study defined as the "reference" threshold. Since the solid overlap always decreases with increasing threshold [Fig. 5(a)], only a decrease with
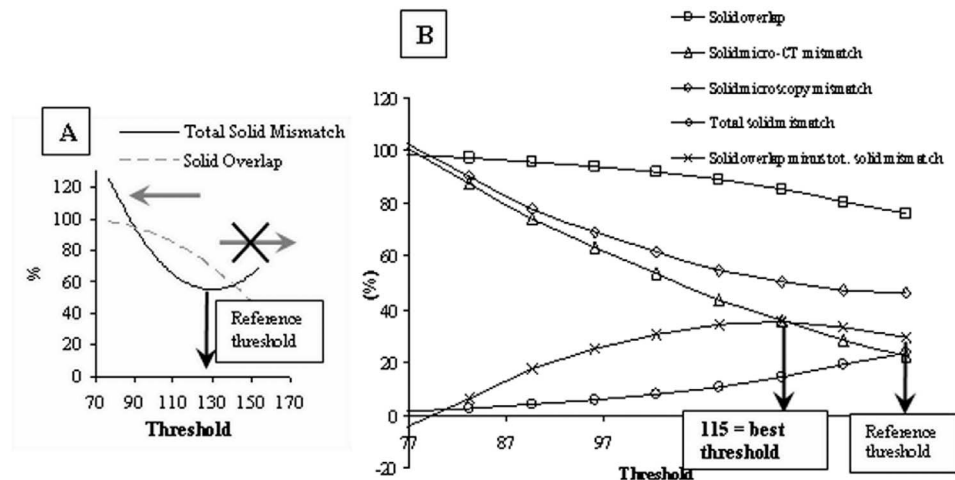

FIG. 5. (A) Definition of the "reference" threshold for one particular image set. Only a decrease in threshold with respect to the "reference" threshold is concerned for the determination of the "best" threshold. (B) Influence of the threshold on the solid overlap, solid microscopic, solid micro-CT and total solid mismatch, the solid overlap minus total solid mismatch, and determination of the 'best' threshold for one particular image set with respect to the "reference" threshold.

respect to the "reference" threshold is considered for determining the "best" threshold per image set. When assessing the 36 image sets, a mean "reference" threshold of 127 ± 6 is found. The values are normally distributed.

Figure 5(b) shows for one particular image set the influence of the threshold on the solid overlap, solid micro-CT mismatch, solid microscopic mismatch, and total solid mismatch. Where the difference between the solid overlap and the total solid mismatch reaches its maximum, meaning a maximum in coinciding and a minimum in noncoinciding solid elements, the "best" threshold is defined being 115 for this particular set. Per image set, the "best" threshold is determined. The 36 "best" threshold values are normally distributed and result in a mean "best" threshold value of 111 ± 6, named the 'optimal' threshold.

C. Match for the "optimal" threshold

The "optimal" threshold is then applied on all 36 image sets for binarization. The mean percentage in solid overlap, solid micro-CT mismatch, solid microscopic mismatch, and total solid mismatch are determined based on Eq. (3)–(6) and are summarized in Table III. The mentioned variables are all normally distributed.

To get an overall view of the error made by micro-CT and binarization, all elements (solid and pore) are accounted for. Again, the "optimal" threshold value is applied to binarize the 36 interpolated micro-CT images. For all 36 image sets the total overlap, total micro-CT mismatch, total microscopic mismatch, and total mismatch are determined according to Eq. (7)–(10) and the results are summarized in Table IV. The mentioned variables are all normally distributed.

D. Influence of the interpolation step

As mentioned before, the difference between the physical cutting angle of the metallographic sections and the reconstruction angle of the corresponding micro-CT images introduces a certain mismatch. The current study diminishes this mismatch by providing a tool to interpolate a micro-CT image under the same angle as the physical cutting angle. To prove the importance of the interpolation step, the proposed protocol is as well performed on not interpolated micro-CT images. Therefore, the micro-CT images resembling the microscopic sections the best are considered for matching.

In total, 18 image sets are assessed for both the interpolated and the not interpolated micro-CT images. A "reference" threshold of 129 ± 7 and 135 ± 15, respectively, and an "optimal" threshold of 113 ± 6 and 113 ± 5, respectively, are found. The resultant total overlap, total micro-CT and microscopic mismatch, and total mismatch are summarized in Table V. It can be seen that, although for both the interpo-

lated and not interpolated micro-CT images the "optimal" threshold remains the same, a larger mismatch is found when no interpolation is performed. Since the interpolation related mismatch depends on the difference between the cutting and the reconstruction angle and since this difference varies between the image sets, more outliers are excluded when no interpolation is performed and the resultant standard deviation still remains larger.

E. Image analysis—solid fraction

The fraction of the solid present in both the microscopic and the corresponding, interpolated micro-CT images is determined by dividing the amount of solid elements by the total amount of elements (solid and pore) in the ROI. The 36 interpolated micro-CT images are binarized using the "optimal" threshold. On average, the *absolute* difference in solid fraction between micro-CT and microscopy is $(4.7 \pm 1.9)\%$. The positive value indicates that micro-CT, when applying the "optimal" threshold for binarization, overestimates the real solid structure by about 5%.

Figure 6 shows the correlation between the fraction of the solid calculated from the micro-CT images and from the microscopic images ($p < 0.001$, Pearson's correlation—t approximation). Pearson's correlation between both shows an r statistic of 0.93. Again, it can be seen that the real solid fraction is overestimated by about 5% absolute in the binarized micro-CT images.

F. Image analysis—strut thickness

Quantification of the PVE for a heterogeneous porous structure with a broad range in strut and pore size is not straightforward and is not the subject of this research. However, to get a global idea of the influence of the PVE in function of the threshold and, additionally, to globally quantify the PVE for the determined "optimal" threshold, a study of the average strut thickness in function of the threshold with reference to the real structure (represented by the microscopic image) is performed. Figure 7 sketches this study. It can be seen that, depending on the chosen threshold, the structure edge shifts towards or away from the real structure.

The 36 interpolated micro-CT images are binarized starting from the "reference threshold," namely, 127, and with decreasing threshold values in steps of 2. Both for the microscopic and the interpolated micro-CT images, the average strut thickness is calculated. Then, since the microscopic image is taken as the reference, the average strut thickness determined for the microscopic images is subtracted from the one of the interpolated micro-CT images and divided by 2 to quantify the PVE. In Fig. 7, this is can be seen as

TABLE III. Mean percentage in solid overlap, solid micro-CT mismatch, solid microscopic mismatch, and total solid mismatch.

Overlap$_{solid}$	$(83.4 \pm 4.5)\%$
$M_{micro\text{-}CT\_solid}$	$(44.2 \pm 9.9)\%$
$M_{microscopy\_solid}$	$(16.6 \pm 4.5)\%$
M_{total_solid}	$(61.0 \pm 8.3)\%$

TABLE IV. Mean percentage in total overlap, total micro-CT mismatch, total microscopic mismatch, and total mismatch.

Overlap$_{total}$	$(89.1 \pm 1.4)\%$
$M_{micro\text{-}CT\_total}$	$(7.8 \pm 1.5)\%$
$M_{microscopy\_total}$	$(2.8 \pm 0.7)\%$
M_{total}	$(10.9 \pm 1.4)\%$

TABLE V. Mean percentage in total overlap, total micro-CT mismatch, total microscopic mismatch, and total mismatch for 18 image sets with and without interpolation of the micro-CT images.

	With interpolation	Without interpolation
Overlap$_{total}$	$(88.5 \pm 2.0)\%$	$(85.2 \pm 4.3)\%$
$M_{micro-CT\_total}$	$(7.9 \pm 1.5)\%$	$(10.0 \pm 3.7)\%$
$M_{microscopy\_total}$	$(2.8 \pm 0.8)\%$	$(4.8 \pm 1.8)\%$
M_{total}	$(11.5 \pm 2.0)\%$	$(14.8 \pm 4.3)\%$

FIG. 7. Influence of the threshold value for the micro-CT images on the overestimation of the strut thickness. This phenomenon is applied for the global quantification of the PVE.

$$PVE\_overestimation = \frac{b(or\ c) - a}{2}$$

Figure 8 shows the results. The overestimation due to the PVE in function of the threshold is quasilinear up to about 60 where it reaches its maximum. When the threshold is further diminished, a minimum is reached at about 47 to increase again with decreasing threshold. The drop in the function is mainly due to the background noise in the micro-CT images which is accounted for in the analysis starting from threshold value 60 and lower. When the "optimal" threshold is applied, namely, 111, an average overestimation due to the PVE of 38.8 μm is found which equals to about 3 voxels. It has to be pointed out that this is only an average value. The PVE will be larger for thin struts and small pores and smaller for features significantly larger than the spatial resolution.

IV. DISCUSSION

When using microscopy for characterizing porous structures, one is limited by its 2D character and a critical, time-consuming sample preparation. Therefore, micro-CT is put forward as the solution for 3D characterization of porous structures. However, to ensure and quantify the reliability and the accuracy of the micro-CT images, a validation protocol is developed by matching micro-CT tomograms to microscopic images. Microscopy is chosen as the "golden stan-

dard" because of its physical character, its well-known procedure, and its better resolution with respect to standard micro-CT. When high resolution micro-CT or nano-CT (standard or synchrotron) images are validated, SEM images can be applied to guarantee a superior resolution with respect to the CT images. The main advantages of the proposed validation protocol are, first, the opportunity to interpolate a micro-CT image under the same angle as the physical cutting angle of the microscopic sections; second, the novel thresholding method; and, third, the more precise and detailed quantification of the visualization and binarization error present in the micro-CT images.

In this study, as a proof of principle, the validation protocol is applied to porous titanium structures. When scanning the samples on a Philips HOMX 161 x-ray system with AEA TOMOHAWK CT software applying the scanning parameters mentioned in Table II and binarizing the micro-CT images with the determined "optimal" threshold, a total overlap of about 89% and a total mismatch of about 11% are found. The total mismatch consists of about 8% total micro-CT mismatch and about 3% total microscopic mismatch. Thus, it is concluded that micro-CT visualizes about 89% of the solid and pore phase correctly. However, the images overestimate the structure by about 8%. Additionally, they do not visualize about 3% of the real structure. Possible reasons for both the overestimation and the inability to visualize some features are elaborated below.

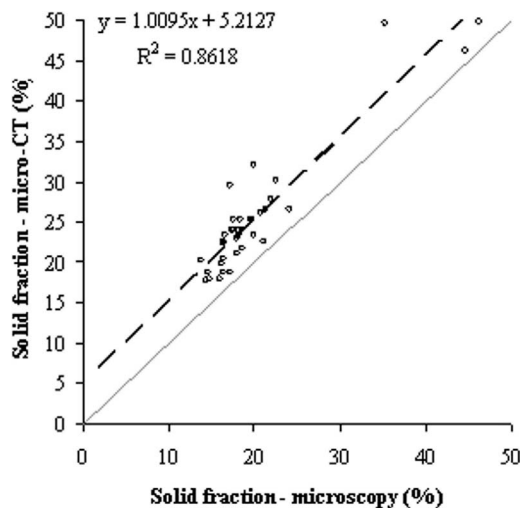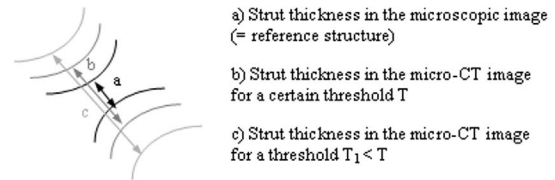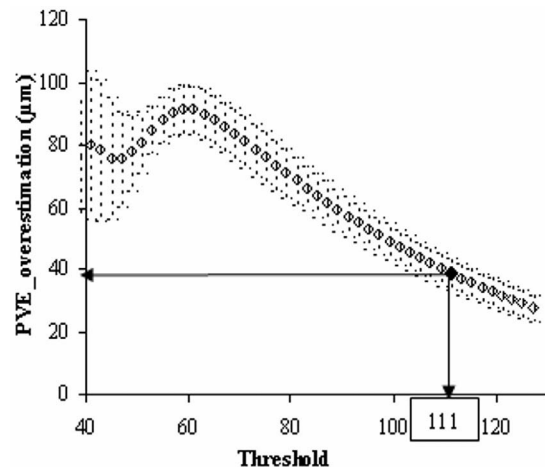It has to be mentioned that, if only the solid fraction

FIG. 6. Correlation between the solid fraction calculated from the microscopic images and the solid fraction calculated from the micro-CT images ($p < 0.001$, Pearson's correlation—t approximation, r statistic=0.93).

FIG. 8. Overestimation of the average strut thickness divided by 2 (PVE_overestimation) in function of the threshold. The "optimal" threshold corresponds to a PVE_overestimation of 38.8 μm (about 3 voxels).

would be considered for validating micro-CT, one would conclude that micro-CT only overestimates the structure by about 5%.

A. Partial volume effect related error

The PVE is implicitly present in micro-CT images. It causes gray values (intensities in the images) to differ from what they ideally should be. For example, micropores in the range of the attainable resolution should ideally be represented by voxels with a gray value of 0, which is not the case due to the PVE. Factors affecting this phenomenon are as follows: (i) the limited spatial resolution, (ii) the size and shape of the struts/pores, and (iii) the image sampling or thickness of the slices. Thus, as will be stated in the next section, the lower the resolution, the more blurring and less sharp the material edges and, hence, the lower the image quality will be. Also, when the features are in the range of the spatial resolution or if the shape is complex, the influence of the PVE is larger (also see Sec. IV D). When the thickness of the micro-CT slices exceeds one cubic voxel, the PVE also plays a role in the third dimension (z direction). To minimize this effect in the current work, the thickness of the micro-CT slices is kept minimal (1 cubic voxel).

B. Resolution related error

The resolution of the micro-CT images is limited not only by the device used, but also by the dimensions of the sample. It is known that, to reduce artifacts and noise, the complete sample width should be in the field of view while scanning. Hence, the resolution of the resulting images is restricted. When the resolution exceeds the dimensions of, for example, micropores or very thin struts, they are not visualized correctly by micro-CT, leading to filling of the micropores and/or a reduction of connecting struts. This gives rise to both an overestimation of the structure and the lack of visualizing small features. Also, since the PVE increases with decreasing resolution, image accuracy goes down.

C. Acquisition and material related error

Due to the high attenuating character of metals, artifacts such as beam hardening, streaks, noise, and PVE are quite pronounced in their micro-CT images. To partially tackle or suppress these artifacts, optimal acquisition parameters are in this study determined by using a micro-CT simulator. However, since not all artifacts can be removed, a mismatch between the micro-CT and the microscopic images exists. Thus, when the material under investigation is known to cause pronounced artifacts or, in addition, when wrong or nonoptimal acquisition parameters are used, a significant mismatch can be expected.

D. Structure related error

The more complex the structure and the broader the range in dimensions of the structural features, the larger the mismatch will get. Indeed, as mentioned before, the closer the feature dimensions approach the attainable spatial resolution, the larger the influence of the PVE and, hence, the larger the mismatch.

E. Interpolation related error

As stated in the Introduction, when histology is used to validate micro-CT and when the physical cutting angle of the microscopic sections does not coincide with the reconstruction angle of the micro-CT images, no interpolation is made. As indicated in literature and proven in this study, this can give rise to an induced mismatch. Also, since the difference between the cutting and the reconstruction angle of the microscopic and the micro-CT images, respectively, is not equal for all image sets, a larger scatter on the results is expected. In the proposed validation protocol, this problem is tackled by providing an interpolation tool to reconstruct an interpolated micro-CT image under the same angle as the physical cutting angle. However, one might think that a small mismatch could be introduced by the interpolation process itself. Therefore, to prove the accuracy and reliability of the interpolation tool, repeated interpolation of one micro-CT image was carried out by different users. For each repetition, the solid overlap and the solid microscopic and micro-CT mismatch were calculated, resulting in a standard deviation of 0.4% for all variables. Additionally, a standard deviation of 0.1% on the absolute difference in surface fraction between the microscopic and the micro-CT image was found. Thus, the interpolation tool is proven to be user independent, objective, and accurate.

F. Threshold related error

The influence of the threshold on the solid overlap, the total solid mismatch, and the absolute difference in solid fraction between the micro-CT and microscopic images is proven to be significant and has to be accounted for.

By the authors' knowledge, currently only one study reports the comparison of the spatial distribution of the solid between microscopic sections and their micro-CT homologs by matching both images instead of comparing structural parameters. Stoppie *et al.*[23] found an overall matching of 89% between micro-CT slices and histological sections of bone around screw-type titanium implants. However, it has to be mentioned that the overall matching was determined on the solid elements only and that the remaining noncoinciding solid elements in the micro-CT images were determined differently compared to this study. When applying the same approach as Stoppie *et al.*, this study results an overall matching of about 83% and a percentage of remaining noncoinciding solid elements in the micro-CT images of about 35%, while Stoppie *et al.* found about 89% and 29%, respectively.

An interstudy comparison can be made since Stoppie *et al.* used the same micro-CT device, applied similar acquisition parameters, had micro-CT images with a similar spatial resolution, and used the same reconstruction algorithms. Also, they analyzed titanium samples. However, those samples, which were surrounded by bone, were of much less complexity. The samples assessed in this study have a much broader range in structural feature dimensions. Hence, as mentioned before, the more complex the structure and the more structural features with dimensions in the range of the spatial resolution, the larger the mismatch between micro-CT

and microscopy. Thus, the results of both studies can be compared taking into account the difference in morphological sample complexity.

V. CONCLUSIONS

For cancellous bonelike structures, literature has already confirmed the ability of micro-CT to image the 3D architecture correctly, and the visualization error inherently present in the micro-CT images is quantified. However, when other porous structures are assessed, literature could not yet provide quantitative data concerning the accuracy and reliability of the micro-CT images. Therefore, in this study, a validation protocol is developed which can be applied to porous materials in general. It compares micro-CT tomograms to microscopic images by matching them and renders parameters to quantify the error made when applying the micro-CT images for further analysis. One of the innovations of the protocol is the opportunity to reconstruct an interpolated micro-CT image under the same angle as the physical cutting angle of the microscopic sections. Also, a novel thresholding method is developed where the optimal threshold is determined at the maximum in coinciding and the minimum in noncoinciding solid elements when overlaying micro-CT and microscopic images.

As proof of principle, the validation protocol is applied to porous titanium structures, scanned on a Philips HOMX 161 x-ray system with AEA TOMOHAWK CT software with a spatial resolution of 27 μm. It is concluded that, despite the morphological complexity of the titanium samples and the variety in structural feature dimensions, a good match is found between microscopy and micro-CT. Additionally, the mismatch is quantified in a detailed manner providing the percentage of overestimation and the percentage of the structure not visualized by micro-CT. It is shown that metal porous structures can be analyzed with sufficient accuracy by means of *standard* micro-CT. However, due to, for example, the limited spatial resolution and the high attenuating character of the metallic samples, a significant mismatch is found which needs to be accounted for when performing image-based structural analysis.

ACKNOWLEDGMENTS

[1] A. H. Benouali, L. Froyen, J. F. Delerue, and M. Wevers, Med. Imaging Technol. **18**, 489 (2002).
[2] R. C. Atwood, J. R. Jones, P. D. Lee, and L. L. Hench, Scr. Mater. **51**, 1029 (2004).
[3] S. V. N. Jaecques, H. Van Oosterwyck, L. Muraru, T. Van Cleynenbreugel, E. De Smet, M. Wevers, I. Naert, and J. Vander Sloten, Biomaterials **25**, 1683 (2004).
[4] A. C. Jones, B. Milthorpe, H. Averdunk, A. Limaye, T. J. Senden, A. Sakellariou, A. P. Sheppard, R. M. Sok, M. A. Knackstedt, A. Brandwood, D. Rohner, and D. W. Hutmacher, Biomaterials **25**, 4947 (2004).
[5] R. A. Ketcham and W. D. Carlson, Comput. Geosci. **27**, 381 (2001).
[6] K. S. Lim and M. Barigou, Food Res. Int. **37**, 1001 (2004).
[7] H. B. Shen, S. Nutt, and D. Hull, Compos. Sci. Technol. **64**, 2113 (2004).
[8] L. Salvo, P. Cloetens, E. Maire, S. Zabler, J. J. Blandin, J. Y. Buffiere, W. Ludwig, E. Boller, D. Bellet, and C. Josserond, Nucl. Instrum. Methods Phys. Res. B **200**, 273 (2003).
[9] G. R. Davis and J. C. Elliott, Mater. Sci. Technol. **22**, 1011 (2006).
[10] S. T. Ho and D. W. Hutmacher, Biomaterials **27**, 1362 (2006).
[11] V. Cnudde, B. Masschaele, M. Dierick, J. Vlassenbroeck, L. Van Hoorebeke, and P. Jacobs, Appl. Geochem. **21**, 826 (2006).
[12] R. Muller, T. Hildebrand, H. J. Hauselman, and P. Ruesegger, Technol. Health Care **4**, 113 (1996).
[13] B. De Man, J. Nuyts, P. Dupont, G. Marchal, and P. Suetens, IEEE Trans. Nucl. Sci. **46**, 691 (1999).
[14] B. De Man, J. Nuyts, P. Dupont, G. Marchal, and P. Suetens, IEEE Trans. Nucl. Sci. **47**, 977 (2000).
[15] J. L. Kuhn, S. A. Goldstein, L. A. Feldkamp, R. W. Goulet, and G. Jesion, J. Orthop. Res. **8**, 833 (1990).
[16] R. J. Fajardo, T. M. Ryan, and J. Kappelman, Am. J. Phys. Anthropol. **118**, 1 (2002).
[17] R. Muller, M. Hahn, M. Vogel, G. Delling, and P. Ruegsegger, Bone (N.Y.) **18**, 215 (1996).
[18] R. Muller, H. Van Campenhout, B. Van Damme, G. Van Der Perre, J. Dequeker, T. Hildebrand, and P. Ruegsegger, Bone (N.Y.) **23**, 59 (1998).
[19] J. A. Stadler, W. Cortes, L. L. Zhang, C. C. Hanger, and A. K. Gosain, Plast. Reconstr. Surg. **118**, 626 (2006).
[20] J. S. Thomsen, A. Laib, B. Koller, S. Prohaska, L. Mosekilde, and W. Gowin, J. Microsc. **218**, 171 (2005).
[21] T. Uchiyama, T. Tanizawa, H. Muramatsu, N. Endo, H. E. Takahashi, and T. Hara, Calcif. Tissue Int. **61**, 493 (1997).
[22] D. Chappard, N. Retailleau-Gaborit, E. Legrand, M. F. Basle, and M. Audran, J. Bone Miner. Res. **20**, 1177 (2005).
[23] N. Stoppie, J. P. van der Waerden, J. A. Jansen, J. Duyck, M. Wevers, and I. E. Naert, Clinical Implant Dentistry and Related Research **7**(2), 87 (2005).
[24] F. Snijkers, S. Mullens, J. Luyten, W. Vandessel, S. Impens, J. Schrooten, and J. Van Humbeeck, Proceedings of the Acers Meeting, Cocoa Beach, Florida, USA, January 2005 (unpublished).
[25] S. Impens, S. Mullens, J. Luyten, I. Thijs, J. Van Humbeeck, T. Van Cleynenbreugel, A. Bakker, F. P. Luyten, and J. Schrooten, Proceedings of the 19th European Conference on Biomaterials, Sorrento, Italy, 11–15 September 2005 (unpublished).
[26] L. A. Feldkamp, L. C. Davis, and J. W. Kress, J. Opt. Soc. Am. A **1**, 612 (1984).
[27] A. Y. Sasov, J. Microsc. **147**, 179 (1987).
[28] A. Y. Sasov, J. Microsc. **147**, 169 (1987).
[29] P. Van Marcke and R. Swennen, Proceedings of the second International Workshop on the Application of X-ray CT for Geomaterials (GeoX 2006), Aussois, France, 4–7 October 2006 (unpublished).
[30] F. Maes, A. Collignon, D. Vandermeulen, G. Marchal, and P. Suetens, IEEE Trans. Med. Imaging **16**, 187 (1997).
[31] F. Maes, D. Vandermeulen, and P. Suetens, Proc. IEEE **91**, 1699 (2003).
[32] M. Ding, A. Odgaard, and I. Hvid, J. Biomech. **32**, 323 (1999).
[33] T. Hara, E. Tanck, J. Homminga, and R. Huiskes, Bone (N.Y.) **31**, 107 (2002).
[34] D. Mitton, E. Cendre, J. P. Roux, M. E. Arlot, G. Peix, C. Rumelhart, D. Babot, and P. J. Meunier, Bone (N.Y.) **22**, 651 (1998).
[35] W. Oh and W. B. Lindquist, IEEE Trans. Pattern Anal. Mach. Intell. **21**, 590 (1999).
[36] N. Otsu, IEEE Trans. Syst. Man Cybern. **9**, 62 (1979).
[37] J. H. Waarsing, J. S. Day, and H. Weinans, J. Bone Miner. Res. **19**, 1640 (2004).
[38] A. P. Sheppard, R. M. Sok, and H. Averdunk, Physica A **339**, 145 (2004).
[39] J. S. Weszka, Comput. Vis. Graph. Image Process. **7**(2), 259 (1978).
[40] M. Sezgin and B. Sankur, J. Electron. Imaging **13**, 146 (2004).
[41] N. R. Pal and S. K. Pal, Pattern Recogn. **26**, 1277 (1993).
[42] S. Rajagopalan, L. C. Lu, M. J. Yaszemski, and R. A. Robb, J. Biomed. Mater. Res. **75**, 877 (2005).
[43] M. Ding, M. Dalstra, C. C. Danielsen, J. Kabel, I. Hvid, and F. Linde, J. Bone Jt. Surg., Br. Vol. **79**, 995 (1997).